Integration of Electrical Resistivity Tomography and Seismic Refraction Tomography to Investigate Subsiding Sinkholes in Karst Areas

Oussama Jabrane, Pedro Martínez-Pagán, Marcos A Martínez-Segura, Francisco Javier Alcalá, Driss El Azzab, Marco D Vásconez-Maza, Mohammed Charroud

To cite this version:

Oussama Jabrane, Pedro Martínez-Pagán, Marcos A Martínez-Segura, Francisco Javier Alcalá, Driss El Azzab, et al.. Integration of Electrical Resistivity Tomography and Seismic Refraction Tomography to Investigate Subsiding Sinkholes in Karst Areas. Water, 2023, 15 (12), pp.1-15. 10.3390/w15122192 . hal-04254905

HAL Id: hal-04254905
https://hal.sorbonne-universite.fr/hal-04254905

Submitted on 23 Oct 2023

water

Article

Integration of Electrical Resistivity Tomography and Seismic Refraction Tomography to Investigate Subsiding Sinkholes in Karst Areas

Oussama Jabrane [1,2,*], Pedro Martínez-Pagán [2], Marcos A. Martínez-Segura [2], Francisco Javier Alcalá [3,4], Driss El Azzab [1], Marco D. Vásconez-Maza [5] and Mohammed Charroud [1]

[1] SIGER Laboratory, Faculty of Science and Technology, Sidi Mohamed Ben Abdellah University, Fez BP2202, Morocco
[2] Departamento de Ingeniería Minera y Civil, Universidad Politécnica de Cartagena, 30203 Cartagena, Spain
[3] Departamento de Desertificación y Geo-Ecología, Estación Experimental de Zonas Áridas (EEZA–CSIC), 04120 Almería, Spain
[4] Instituto de Ciencias Químicas Aplicadas, Facultad de Ingeniería, Universidad Autónoma de Chile, Santiago 7500138, Chile
[5] UMR 7619 METIS, CNRS, EPHE, Sorbonne Université, 75005 Paris, France
* Correspondence: oussama.jabrane@usmba.ac.ma

Abstract: Operational and safety issues associated with subsiding sinkholes in karst areas start with the definition of fractures and joints, causing ground weakness. Conventional geotechnical boreholes and geological mapping must be complemented with indirect subsurface exploration techniques to detail those structures. This work aims to use electrical resistivity tomography (ERT) and seismic refraction tomography (SRT) near-surface geophysical techniques to infer the 2D and 3D geometry of sediment-infilled sinkholes formed by the conjunction of fractures and joints in karst areas. Geophysical surveys were performed in a sediment-infilled sinkhole area with two sectors of different subsiding and infilling degrees formed by the conjunction of two fault systems in an experimental research area in the Sierra de Gádor Mountains in southeastern Spain. The ERT survey delimited the geometry of the sinkhole area, including the main fault-boun4ded limits, other minor faults, buried epikarst forms, and the distribution of coarse and clay-rich infilling. The SRT survey corroborated the structure and disambiguated clay-rich and high-moisture-content structures giving similar velocity fields. The integration of the ERT and SRT techniques provides indirect 2D and 3D visualizations of the ground of interest in predicting weakness-triggering mechanisms associated with the regional karst structure. This trial in an experimental uninhabited area, with the possibility of exploring subsiding karst structures is of special interest for designing operational and safety measures in urban areas, where similar karst structures may go undetected and monitoring capability is often more limited. The technological development of the used techniques enables the periodical geophysical monitoring of karst structures, thus making the identification of structural changes modifying the land safety and hydrological mechanisms feasible over time.

Keywords: subsiding karst structures; ground safety; electrical resistivity tomography; seismic refraction tomography; Sierra de Gádor mountains; Spain

Citation: Jabrane, O.; Martínez-Pagán, P.; Martínez-Segura, M.A.; Alcalá, F.J.; El Azzab, D.; Vásconez-Maza, M.D.; Charroud, M. Integration of Electrical Resistivity Tomography and Seismic Refraction Tomography to Investigate Subsiding Sinkholes in Karst Areas. *Water* **2023**, *15*, 2192. https://doi.org/10.3390/w15122192

Academic Editor: Lluís Rivero

Received: 31 March 2023
Revised: 3 June 2023
Accepted: 6 June 2023
Published: 10 June 2023

1. Introduction

In karst landscapes, downward vertical movement of rainfall and surface water through sinkholes, ponors, and poljes produces concentrated, rapid infiltration. It can also occur through faults and joints as preferential infiltration, or through the soil as diffuse infiltration. This network of conducts can also transmit water horizontally to points of concentrated seepage or to major discontinuities after some near-surface storage. Therefore, the study of epikarst structures is necessary for understanding the mechanisms of rainfall infiltration and subsequent carbonate rock dissolution, clay-rich infilling, and associated processes such as land subsidence causing damage [1,2].

Sinkholes, also known as dolines, are surface karst landforms formed in weakened areas by a conjunction of fractures and joints. They identify areas of preferential dissolution of soluble rocks such as limestone and gypsum, which can evolve to produce land subsidence and/or collapse. Although unimpressive and often well-integrated into the landscape, these landforms are frequently linked to the hydrological system and can be reactivated. Their geological characterization is essential to assess the geological hazard during potential future development. Several classifications and terminologies of sinkholes have been published [3–10]. Each one of them describes the form of subsidence or collapse mechanisms involved in their developments in different lithology types, characterizing the particular karst features where they represent the most dangerous geohazard [8,9,11,12].

Near-surface geophysics techniques have proven reliable to detect hidden karst forms, such as cavities, poljes, and sinkholes causing damage. Accurately detecting these forms is essential to assess the safety of new infrastructures, understand the processes involved in their occurrence, and predict future potential development. Compared to the detection of air [13–15] and water-filled cavities [16–19], whose physical properties can be very different from those of the surrounding rocks, the detection of cavities and sinkholes infilled with detrital sediments becomes a complex task requiring the geological complexity of the region and the processes controlling the rock dissolution to be considered. Historical changes observed in sinkhole distribution, geological environment, drilling data, local subsidence rates, analysis of aerial photographs, and site inspection [20–24] are required actions before choosing and planning the proper geophysical survey.

Technical advances in field surveys have allowed a more efficient use of near-surface geophysical techniques and they are becoming less time-consuming and cheaper than classic geotechnical techniques. New software for data processing has also facilitated multiple manipulations for better, faster, and more accurate outcome readings [25,26]. Nevertheless, the correct interpretation of results is not achievable without knowing the geological structure and involved karst processes, which themselves, in turn, determine the choice of the most appropriate geophysical techniques in each case.

Many experiences have reported integrated uses of ERT and SRT near-surface geophysical techniques as a way to disambiguate complex ground structures for different research purposes. In karst areas, the ERT technique solved well the electrical resistivity contrast between carbonate rocks, sedimentary clay-rich infilling, and variable water content resistivity fields. The large experience of the ERT technique in karst exploration [27–29] contrasts with the few experiences of the SRT technique [30–33]. This is due to the limitation of the SRT technique to produce confident results when the layer's stiffness does not increase with depth [34]. The presence of any inclusion of such cavities and sinkholes with lower stiffness can be misinterpreted.

This work delves into the feasibility of integrating the ERT and SRT techniques to infer the 3D geometry of sediment-infilled sinkholes formed by the conjunction of faults and joints in karst areas. Since achieving this goal in urban areas can be subjected to important constraints leading to uncertain interpretations due to (i) electrical and electromagnetic interferences, (ii) limited space to conduct geophysical services, and (iii) incapability of monitoring stationary and transient ground features, an isolated karst area having well-known geology and soil properties was chosen. Exploration depth with enough resolution of these and other near-surface geophysical techniques is limited to some dozen meters at most [35,36]; thus, other deeper features such as the connection of vertical karst forms, the termination of faults generating the sinkhole areas, and total sediment infilling were not subjects of this work.

2. Study Area

The Sierra de Gádor Mountains (peak elevation 2246 m a.s.l.) is a 670 km^2 Mediterranean semiarid to subhumid carbonate range located in the southwest part of the Almería province in southeast Spain, between 36°40′ N to 37°01′ N and 2°30′ W to 2°59′ W (Figure 1a). It is the main recharge area for the deep, productive aquifers in the Campo de Dalías [37,38], which is a 360 km^2 semiarid coastal plain intensively exploited for groundwater to irrigate 260 km^2 of greenhouses and supply the urban areas [39].

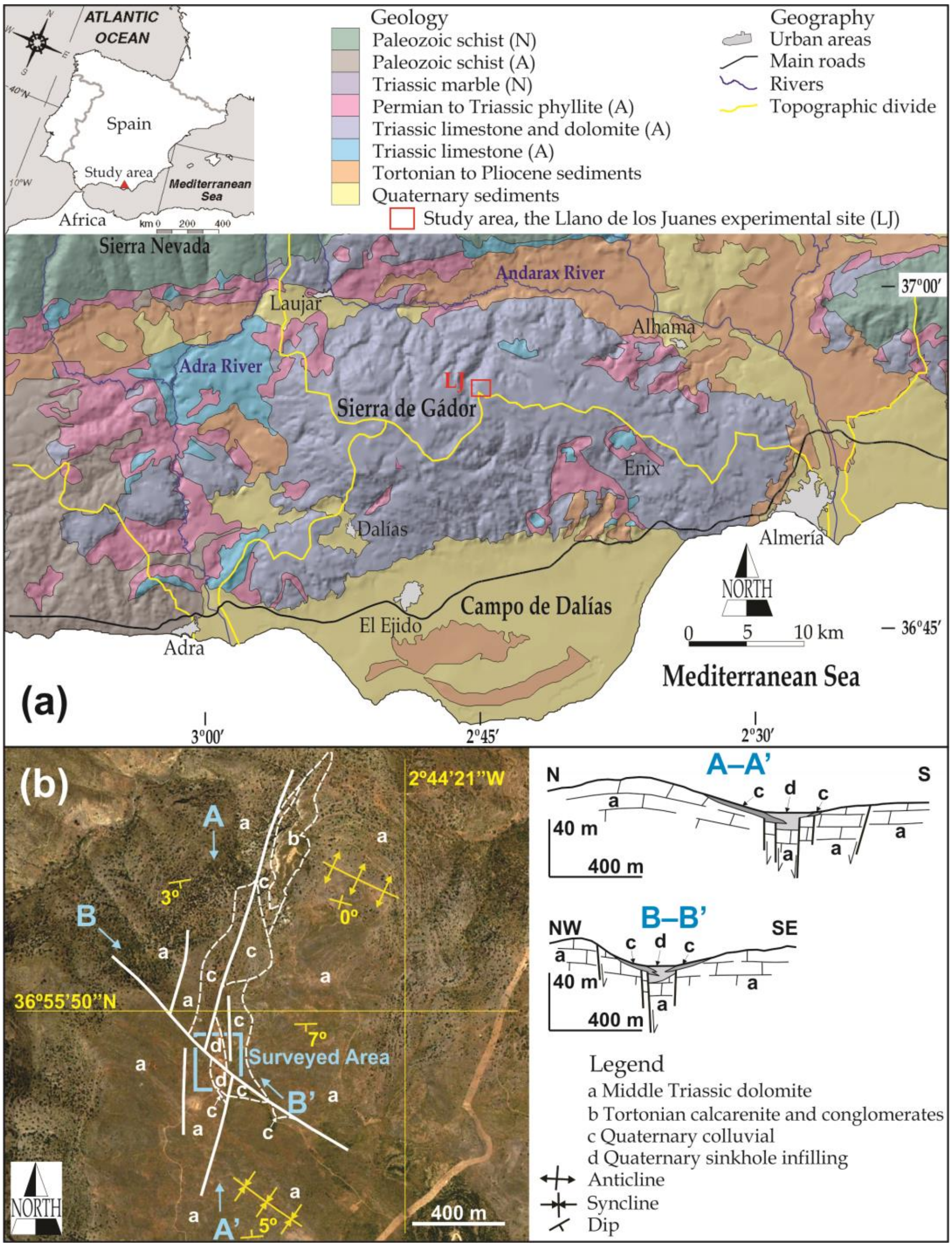

Figure 1. (**a**) Location of the Sierra de Gádor Mountains in Almería province over a 50 m resolution digital elevation model. Regional geology (1:100,000 scale) simplified and updated from [40]; Nevado–Filabride (N) and Alpujárride (A) tectonic complexes of the Internal Zone of the Betic Chain. (**b**) Detailed geological sketch and cross-sections A–A′ and A–B′ (1:5000 scale) over a satellite image (source Google Earth) of the sinkhole area studied in the Llano de los Juanes experimental site, also indicating the surveyed area as in Figure 2.

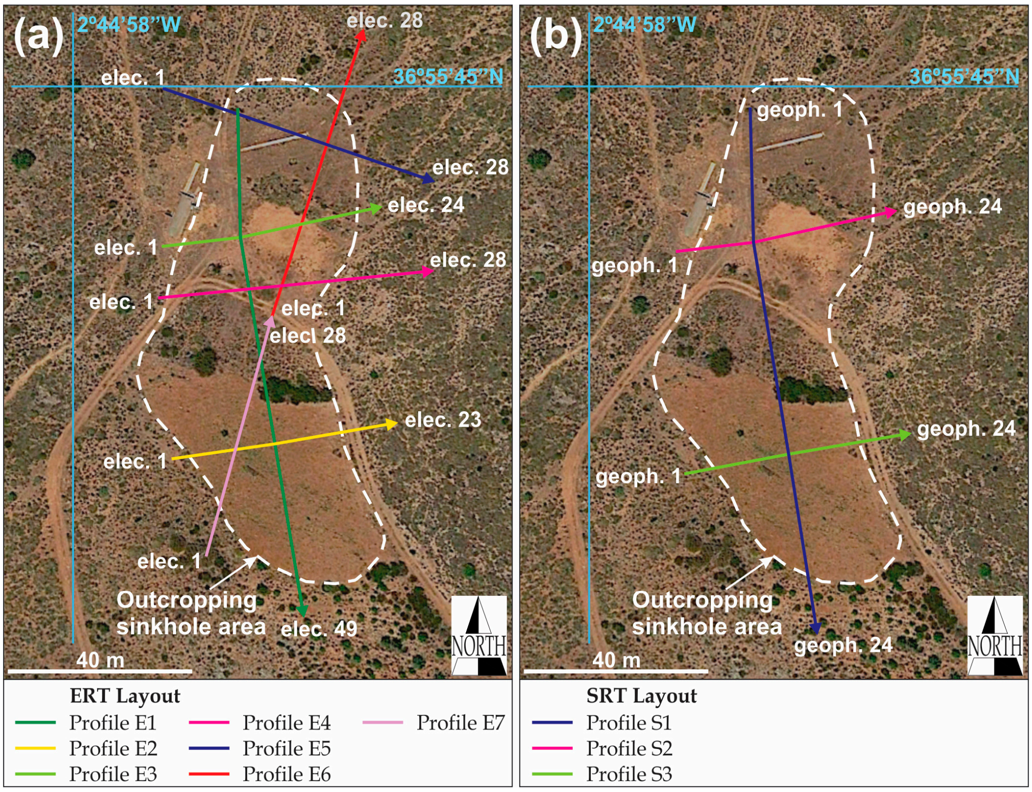

Figure 2. Satellite image (source Google Earth) of the sinkhole area surveyed in the Llano de los Juanes experimental site, including the location of the (**a**) seven ERT profiles E1 to E7 (indicating the number and disposition of electrodes (elec.) used in each one) and (**b**) three SRT profiles S2 to S3 (indicating the number and disposition of geophones (geoph.) used in each one).

The Sierra de Gádor Mountains consist of a thick series of Triassic limestone and dolomite, underlain by Permian to Triassic metapelites belonging to the Gádor and Félix Units of the Alpujárride Tectonic Complex, Internal Zone of the Betic Chain [40]. This Triassic carbonate formation continues under the Campo de Dalías coastal plain overlain by Miocene to Pliocene calcarenites and marls and Quaternary colluvial [41,42]. The area is tectonically active as a consequence of the convergence between the African and Eurasian Plates, which ended with the collision of the Internal and External Betic domains during the early Miocene [43]. Active tectonics and sea-level changes control the space for the Neogene–Quaternary sedimentation [44]. The inherited compressional regional structure identifies the Sierra de Gádor as a great anticline and the Campo de Dalías as a great syncline [40,42]. The dense net of flexural distensive fracturing in the hinge zone associated with the Triassic carbonate anticline determines several structural karst forms in the summit and slopes of the Sierra de Gádor Mountains, including sinkholes.

The Llano de los Juanes experimental site is a sinkhole area of structural origin that forms an endorheic flat-summit basin of 15 hectares at 1600 m elevation (Figure 1b). This site has been investigated over the last three decades for different environmental subjects [38,45,46]. The soil is Lithic Haploxeroll–Lithic Ruptic Argixeroll [45], thin (average 35 cm) and discontinuous over limestone bedrock, and clayey with 40–59% silt and 21–68% clay. Soil organic matter content ranges from 1.3% to 7.3%, mean bulk density is 1.1 $\mathrm{g/cm^{-3}}$, and the unsaturated hydraulic conductivity is 1.5–1.6 mm $\mathrm{h^{-1}}$ at 120 mm water tension and 12–194 mm $\mathrm{h^{-1}}$ at 30 mm water tension [47,48]. The surveyed sinkhole area is N–S elongated and includes two sectors, a northern one that is 30 m wide and 50 m long and a southern elongated one that is 40 m wide and 70 m long (Figure 2). The sinkhole infilling includes reddish clay-rich "terra rossa" sediments and coarsely grained colluvial with a clay-rich matrix sourced from adjacent reliefs. The bedrock formation is

Triassic dolomite from the Gádor–Turón Unit. The feeding zone comes from the E and W slopes and the southern area in the case of the northern sector. The sinkholes receive direct rainfall and surface runoff from the E and W slopes. The combination of clayed infilling and surface-water feeding after rainfall events prevents a permanent vegetation cover within the sinkhole area.

3. Methods

3.1. ERT Technique and Arrays

Electrical resistivity tomography (ERT) is a non-invasive geophysical technique widely used for subsurface investigation [49,50]. The technique reconstructs the distribution of electrical resistivity (hereafter ER) data in the region below the acquisition line [51]. ERT is a combination of electrical techniques, allowing to characterize the horizontal and vertical variations of ER [52].

ER data were acquired using a SuperSting R8 equipment from Advanced Geosciences Inc. (AGI, Austin, TX, USA) (Figure 3a) with a multi-electrode device to acquire different measurements for each of the different combinations of four electrodes and a dipole-dipole array configuration. This array is more sensitive to lateral changes of ER than to vertical changes. Therefore, its response to vertical structures is better than that for horizontal structures [53]. All the ER pseudo sections were inverted using the Earthimager 2D software v.1.9 [54]. The smooth fitting model was the inversion process mode chosen because of its robustness at dealing noisy values. For accurate data inversion, at least five interactions were performed and a root-mean-square error (RMS) of less than 6% was set as standard.

Figure 3. Visual documentation of equipment and operations in the field. (**a**) ERT survey using SuperSting R8 equipment from AGI. (**b**) Executed hammer blow (the shot) to generate seismic waves in an SRT survey. (**c**) SRT survey using SUMMIT II Compact equipment from DMT. (**d**) Checking of the electrodes (ERT surveys) and geophones (SRT surveys) for data acquisition.

Resistivity data were collected in seven ERT profiles labeled as E1 to E7 (Figure 2a). Profile E1 (120 m long) was N–S oriented, profiles E6 and E7 were laid out following the NNE–SSW direction according to a roll-along [55] design with a total length of 132 m, and profiles E2 to L5 were E–W oriented and perpendicular to the profile E1. This arrangement was designed to ensure comprehensive coverage and a well-rounded assessment of the study area. To ensure consistency and comparability across profiles, we used a standardized electrode spacing of 2.5 m throughout the survey (Figure 3d). Figure 2a shows the location, orientation, and number of electrodes used in each profile.

3.2. SRT Technique and Arrays

The seismic refraction tomography (SRT) technique provides information on the mechanical behavior of materials [56]. It consists of generating vibrations on the ground surface (Figure 3b) and measuring the propagation and speed of the different waves emitted [57]. The technique uses the compression waves (P waves) refracted at the top of the layers. The P-wave velocities (V_P) are calculated by measuring the arrival time of the first refracted waves, after the direct arrivals [58].

The used data were travel times of the first waves arriving at the geophones, i.e., the P waves. The V_P data were acquired using SUMMIT II Compact equipment from DMT (Essen, Germany) (Figure 3b,c). It consists of a twenty-four-channel box housed in a solid metal casing. The system incorporates the SUMMIT 'Plug & Trace' technology, which enables easy setup and operation in any environment, ensuring high-speed production [59]. Pseudo-2D DeltatV generates systematic imaging artifacts in case of strong lateral velocity variation on the near surface. The Rayfract software v.3.35 by Intelligent Resources Inc. (Reading, UK) was used to create 2D models of V_P, reproducing the travel times of the measured waves, called first breaks. In this way, refractors are inferred with the conventional reciprocal method [60]. To determine the arrival times of the first wave for each geophone and shot, a manual picking process was used. P-wave arrivals were specifically recorded, and their corresponding first arrival times were manually identified. Figure 4 depicts the wave path coverage for the S2 profile, displaying an example of recorded P-wave arrivals with manually picked first arrival times, and showcasing the spatial distribution of the five shots.

Forward finite difference modeling to estimate the travel times between shots and geophones and the ray paths were used. Modeled and observed travel times can be fitted by iteratively adjusting V_P nodal data pairs [61]. The calculation method called Wavepath Eikonal Traveltime inversion (WET) [62] was used to model the V_P distribution of the subsurface used, which were "fat rays" or Fresnel volumes for modeling of first break energy transport, instead of conventional "thin rays" assuming finite frequency and correctly modeling loss of resolution with increasing distance from source/receiver due to widening of wave path/Fresnel volume [63].

V_P data were collected in three SRT profiles labeled as S1 to S3 (Figure 2b). Profile S1 was N–S oriented and profiles S2 and S3 were E–W oriented and perpendicular to the profile S1. All profiles used 24 vertical geophones. Geophone spacing was 5 m in S1 and 2.5 m in S2 and S3. Five ground shots were conducted along each profile, resulting in propagating ground waves that were recorded by each geophone. A stacking approach was used to improve the signal quality and reduce the influence of noise.

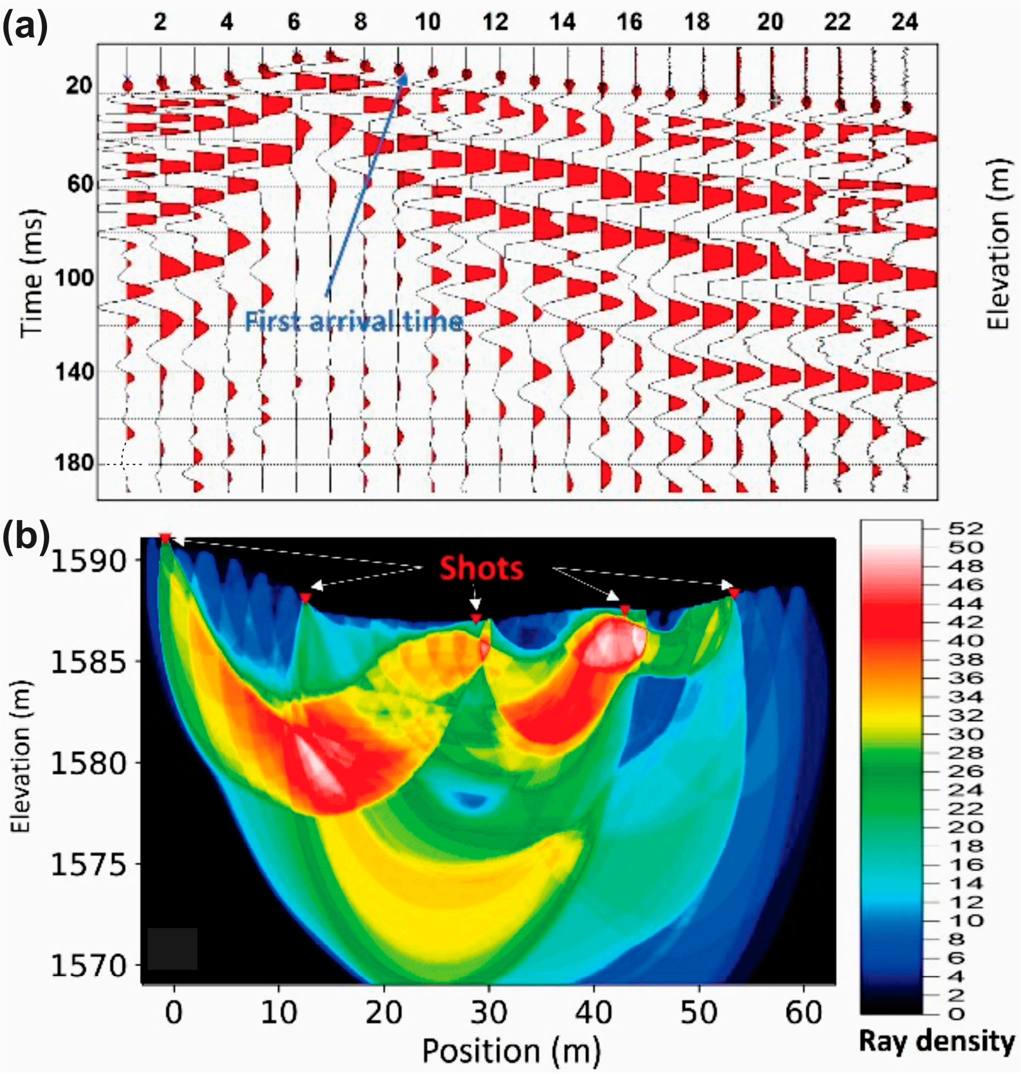

Figure 4. (**a**) SRT shots recorded during the S2 profile acquisition with the corresponding first arriving time for each geophone. (**b**) Raypath coverage for the S2 profile.

4. Results and Discussion

4.1. ERT Surveys

The seven inverted ERT profiles (labeled E1 to E7; Figure 2a) used the dipole-dipole array configuration and a 2.5 m electrode spacing (Figure 5). Other operational field conditions, as well as the number of iterations, used the "L norm" regularization to control the smoothness, and RMS values calculated are summarized in Table 1.

Table 1. Summary of ERT surveys characteristics.

Profile	Length, m	Depth, m	Spacing, m	L Norm	Iterations	RMS, %
E1	120	26	2.5	0.92	5	2.88
E2	60	12	2.5	1.20	8	3.28
E3	60	12	2.5	0.94	5	2.90
E4	70	12	2.5	3.52	7	5.63
E5	70	15	2.5	3.63	6	5.72
E6	70	14	2.5	3.22	6	3.22
E7	70	15	2.5	1.87	7	4.11

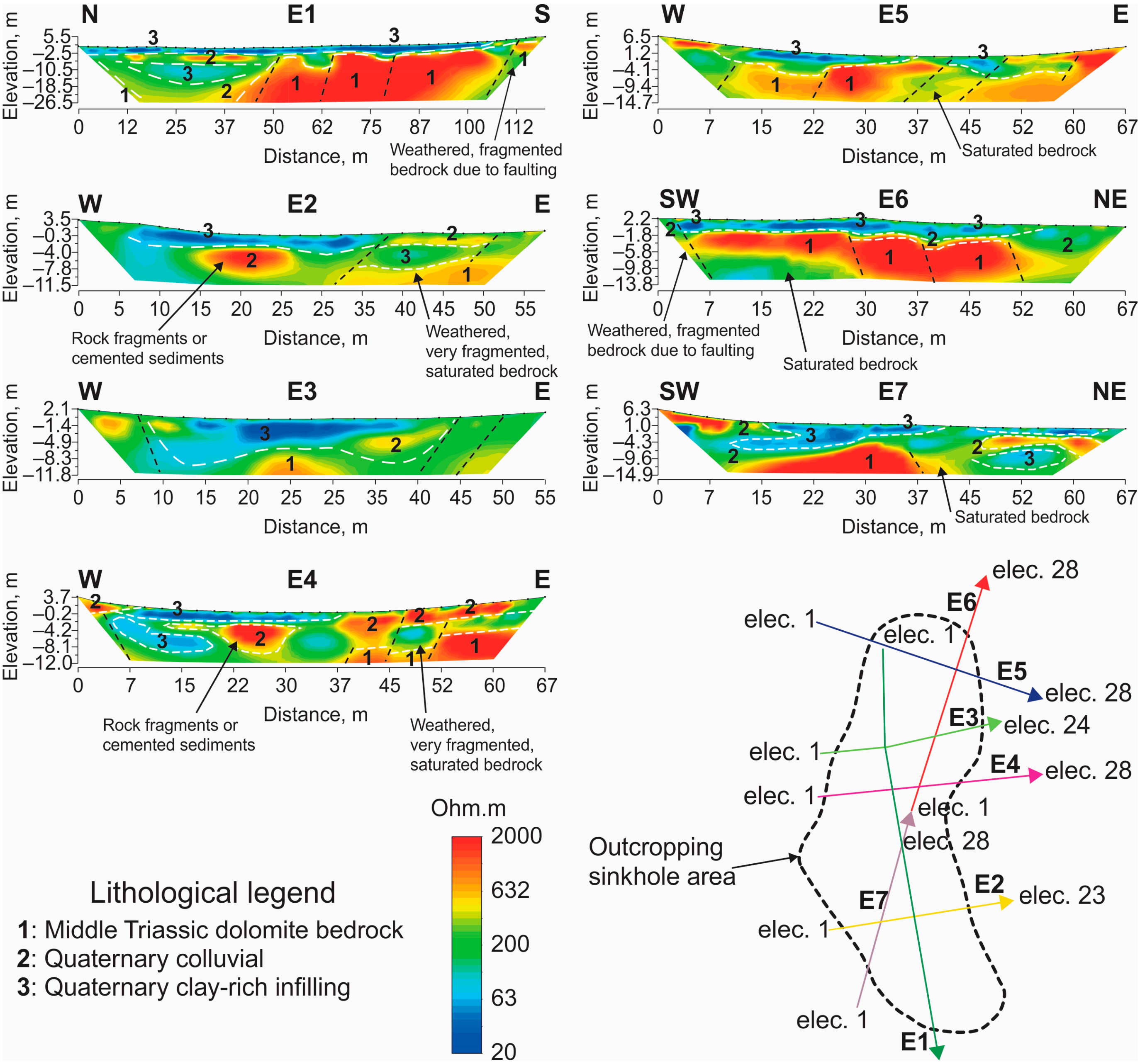

Figure 5. Inverted 2D electrical resistivity models E1 to E7 and their locations as in Figure 2a; see their characteristics in Table 1.

Profiles E1, E6, and E7 were N–S oriented to cover the whole outcropping sinkhole area (Figure 2a; Table 1); they intersected the SE–NW fault system identified in Figure 1b. Profiles E2 to E5 were E–W oriented to identify the sinkhole area lateral boundaries; they intersected the NE–SE fault system identified in Figure 1b. All profiles exhibited RMS values in the 2.88–5.72% range (Table 1).

Profile E1 was intended to identify the northern sinkhole area termination, which was unknown in the field since it is covered by colluvial debris (Figure 1b). It revealed three distinctive ER ranges interpreted as three resistive regions (Figure 5). The first region consists of a relatively homogeneous subsurface layer in the 0–3 m depth with ER in the 14–40 Ωm range, which corresponds to reddish clay well distributed over the entire profile. Below, a well-marked limit in the center of the profile is distinguished, which is attributed to a fracturing zone delimiting two sinkhole sectors showing different karstic development. In the northern sector, a clear subsiding area is marked by ER values in the 100–400 Ωm range. The marked difference in RE values between subsurface (higher ERs) and surface (lower ERs) formations is attributed to colluvial debris. The southern sector shows ER values between 500 Ωm and 2000 Ωm; the higher ER values are related to the intact dolomite rocks. This sector has the form of a pillar over-hanging the alteration corridor, the boundary of which corresponds to a fracturing limit. According to field observations, the sinkhole boundaries have several microfractures and joints, so they are privileged infiltration zones.

Profiles E6 and E7 (Figure 2a; Table 1) were laid out according to a roll-along design starting from E6 to E7 to cover the northern and southern sinkhole area end, respectively. They are interpreted as a continuous one (Figure 5). ER values vary from 20 Ωm to 2000 Ωm. From top to bottom, there are three resistive areas associated with three different layers as (i) a homogeneous and conductive surface layer with low ER values (<50 Ωm in E6 and around 50 Ωm in E7) associated to the clay-rich soil; (ii) a layer with intermediate ER values (50–300 Ωm in E6 and 20–150 Ωm in E7) associated to colluvial debris with higher ER fields, probably due to embedded dolomite layer fragments and/or cemented sediments (paleo soils); and (iii) a bottom layer with ER values up to 2000 Ωm associated to the dolomite unit. As shown in Figure 5, profiles E6 and E7 identify well the two sinkhole sectors, a northern subsiding one that progressively is covered by different sediments and a southern proto-subsiding one with the stable dolomite formation under an initial stage of structuring. The boundary between them is marked by the action of a fracture interpreted from geophysical data, also identified in profile E1.

Ordered from N to S, profiles E5 and E3 surveyed the northern sinkhole sector, profile E4 surveyed the boundary between northern and southern sinkhole sectors, and profile E2 surveyed the southern sinkhole sector. As deduced from the above N–S oriented profiles E1, E6, and E7, the boundary between the sinkhole sectors is characterized by a fault. Profiles E2 to E5 identifies the same above-inferred three main layers associated with the above-identified three main ER areas. From top to bottom, there are also (i) an homogeneous and conductive surface layer with low ER values (20–50 Ωm in E2 and E4, around 50 Ωm in E3 and E5) associated with the clay-rich soil; (ii) a layer with intermediate ER values (150–400 Ωm with in all the E–W oriented E2 to E5 profiles) associated with colluvial debris with higher ER fields, probably due to embedded dolomite unit fragments and/or cemented sediments (paleo soils) with ER values higher than 1000 Ωm; and (iii) a bottom layer with ER values up to 2000 Ωm associated with the dolomite layer, which is locally weathered and/or fractured by faults, giving localized ER vales in the 200–600 Ωm range, probably associated with a subsequent more favorable condition for water saturation. These E–W-oriented E2 to E5 profiles showed a well-defined shape of the eastern and western sinkhole area boundaries by an eastern minor fault structure and a western major fault structure, respectively. The idea of subsurface water drainage and buried epikarstic forms is also justified by the shape of some low RE values associated with the dolomite layer, defining pseudo-horizontal layers due to weathering and pseudo-vertical patches along the external boundary of the fault systems.

The 3D model grid (Figure 6) obtained by intersecting the seven ERT profiles offers a visual representation of the subsurface structure in the studied area. This model effectively captures the subsoil characteristics, including the detection and delineation of significant fractures, as well as the characterization of the shape of the underground karst, particularly the two sinkholes. The interpretation of 3D ERT images relies on analyzing the distribution and contrasts in electrical resistivity.

The E1 profile, the longest and deepest, intersects with three other profiles in its northern section, clearly delineating the sinkhole structure. This intersection between profiles E3, E4, and E7 confirms the consistency of the results, providing further evidence of the presence of the sinkhole. The low resistivity values observed in these profiles are attributed to the conductive clay material filling the sinkhole. Similarly, the southern end of the E6 profile, where the second sinkhole is located, is distinctly identified by its intersection with the central part of the E4 profile. Additionally, the intersection between E2 and E7 profiles highlights the presence of this sinkhole shape. The high resistivity values in the 3D grid also correlate well, indicating agreement at the intersection of the 2D ERT profiles. This pattern is consistently observed throughout ERT profiles E6 and E7, further emphasizing the high resistive nature attributed to the carbonate formation.

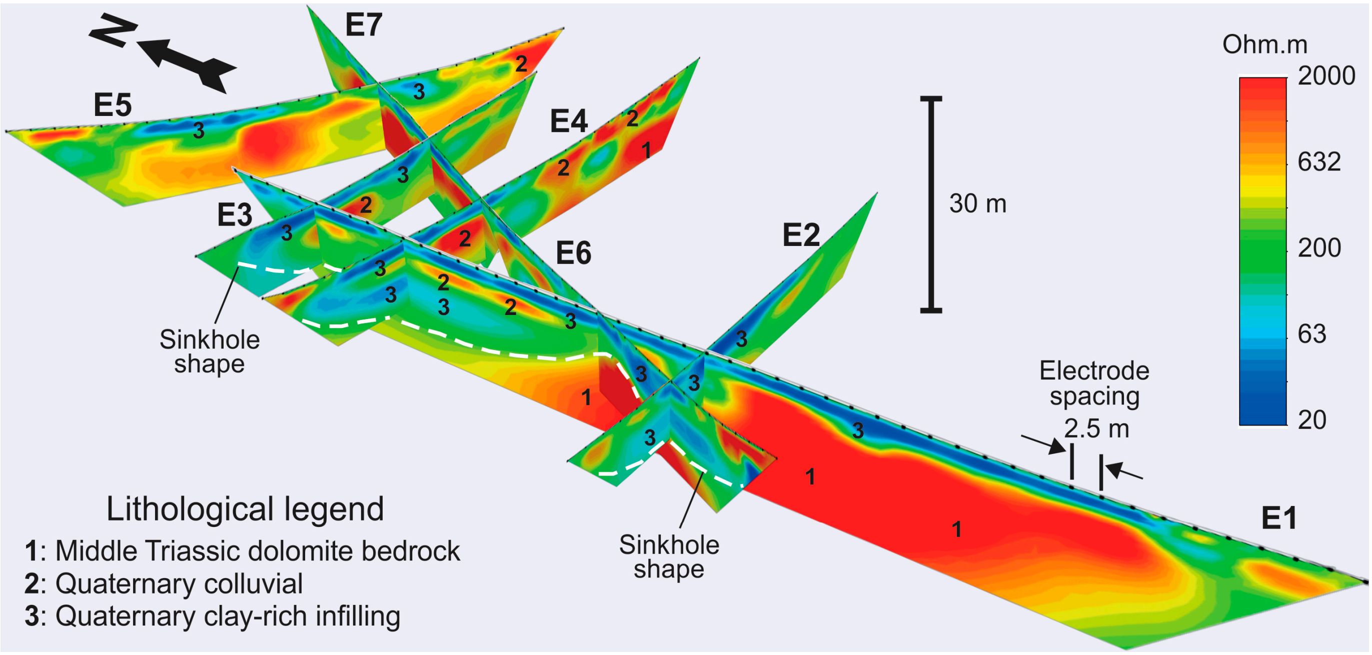

Figure 6. Inverted 3D electrical resistivity model integrating profiles E1 to E7; see location of ERT models in Figure 2a and their characteristics in Table 1.

4.2. SRT Surveys

The final SRT models were obtained after 20 WET iterations of data processing and refinement, resulting in a well-fitted representation of the raw data (RMS < 6%) (Figure 7). The datasets from the three *P*-wave SRT profiles were processed with a specific focus on characterizing the lateral variation of materials, estimating the thickness of layers, including the red clay filling material and the dolomite formation contact. Additionally, the analysis aimed to determine the shape of the sinkhole and identify its boundaries.

The 3D grid analysis of the SRT profiles (Figure 7) illustrates the interpreted V_P models for cross-sections S1, S2, and S3. The depth of investigation for all the inverted datasets spanned from 20 m to 25 m, which proved suitable for characterizing the clay filling materials, colluvial debris, and the dolomite rocks. Thorough examination of all cross-sections reveals distinct velocity characteristics associated with different materials present within the studied area. Low velocity values are specifically observed within the red clay filling materials. The relatively loose and unconsolidated nature of the clay allows for slower seismic wave propagation, which accounts for the low velocity values. Anomalies with high velocity values are found within the red clay, indicating the presence of colluvial debris. These anomalies point to the accumulation of denser materials within the clay, which have higher seismic velocities than the surrounding clay matrix. In the third sector, the higher velocity values are directly associated with the presence of intact dolomite layer. This sector exhibits a pillar-like shape that overhangs the alteration corridor. The boundary of this sector aligns with the limit defined by fracturing, indicating the structural demarcation between the intact bedrock and the surrounding altered formations.

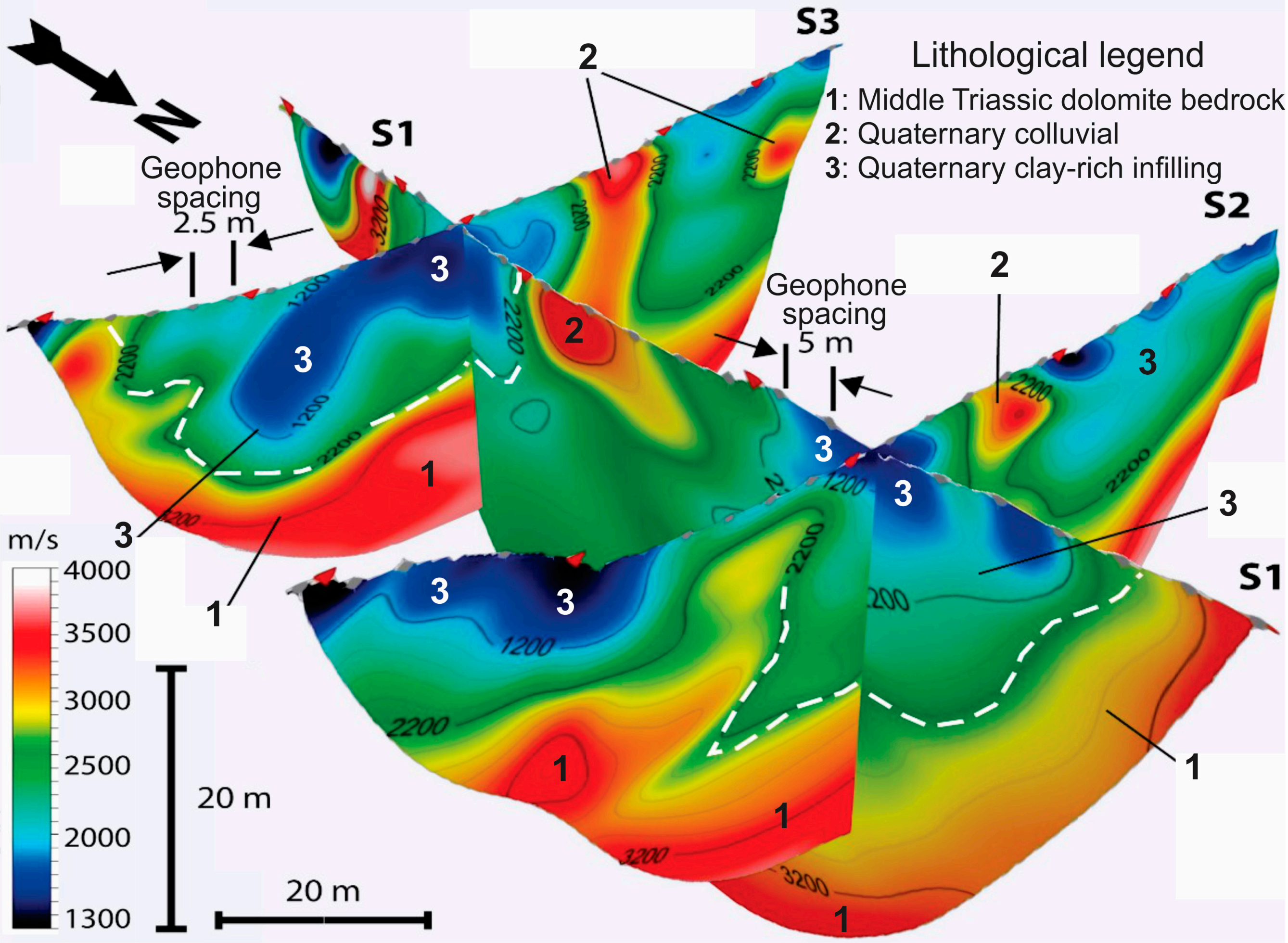

Figure 7. Inverted 3D grid generated by integrating seismic refraction tomography models S1 to S3. See location of SRT models in Figure 2b and their characteristics in Table 2.

Table 2. Summary of SRT surveys characteristics.

Profile	Length, m	Depth, m	Geophones	Spacing, m	Iterations	RMS, %
S1	100	25	24	5	20 WET	2.7
S2	60	20	24	2.5	20 WET	4.2
S3	60	20	24	2.5	20 WET	5.7

Profiles S2 and S3 (Figure 2) were laid out to highlight the contact with S1 and to cover the northern and southern sinkhole area end, respectively. From top to bottom, there are three velocity areas associated with three different layers as (i) a homogeneous surface layer which punctually shows low V_P values (<1200 m/s) associated with the clay-rich soil; (ii) a second layer beneath the first layer is observed with higher velocities ranging from 2500 m/s to 3000 m/s (Vp) due to the embedded dolomite rocks fragments and/or cemented sediments. This second layer exhibits variable thickness throughout the area of interest, associated with colluvial debris; and (iii) at greater depths in the seismic cross-sections, there is a bottom layer characterized by P-wave velocities ranging from 3000 m/s to over 4000 m/s. The isocontour of this high-velocity layer exhibits significant variability, which is attributed to the presence of the dolomite layer.

The 3D SRT grid presented in Figure 7 clearly illustrates the identification of two sinkhole sectors through profiles S2 and S3. These profiles provide valuable insights into the characteristics of these sectors. The northern sector is depicted as a subsiding area gradually covered by various sediment layers. On the other hand, the southern sector is recognized as a proto-subsiding region with a stable dolomite layer undergoing initial structural changes. The boundary between these sectors is defined by the presence of a fracture, which is also evident in profile S1.

In addition, we conducted a qualitative comparison of the refraction seismic and electrical resistivity survey results, focusing on the cross-sections E2, E3, S2, and S3. We achieved a comprehensive understanding of subsurface properties by comparing these SRT and ERT profiles, allowing for more precise geological interpretations. Figure 8 depicts the findings, which revealed a strong correlation between these profiles. The seismic *P*-wave velocity and electrical resistivity values were remarkably comparable. For the filling red clay materials in the subsurface, the resistivity and velocity values showed a coherent relationship. Furthermore, relevant velocity and resistivity values were observed for the colluvial debris deposits within the homogeneous, conductive clay layer, as well as the underlying dolomitic bedrock. This convergence of results further enhances our understanding of the geological characteristics and subsurface composition within the investigated area.

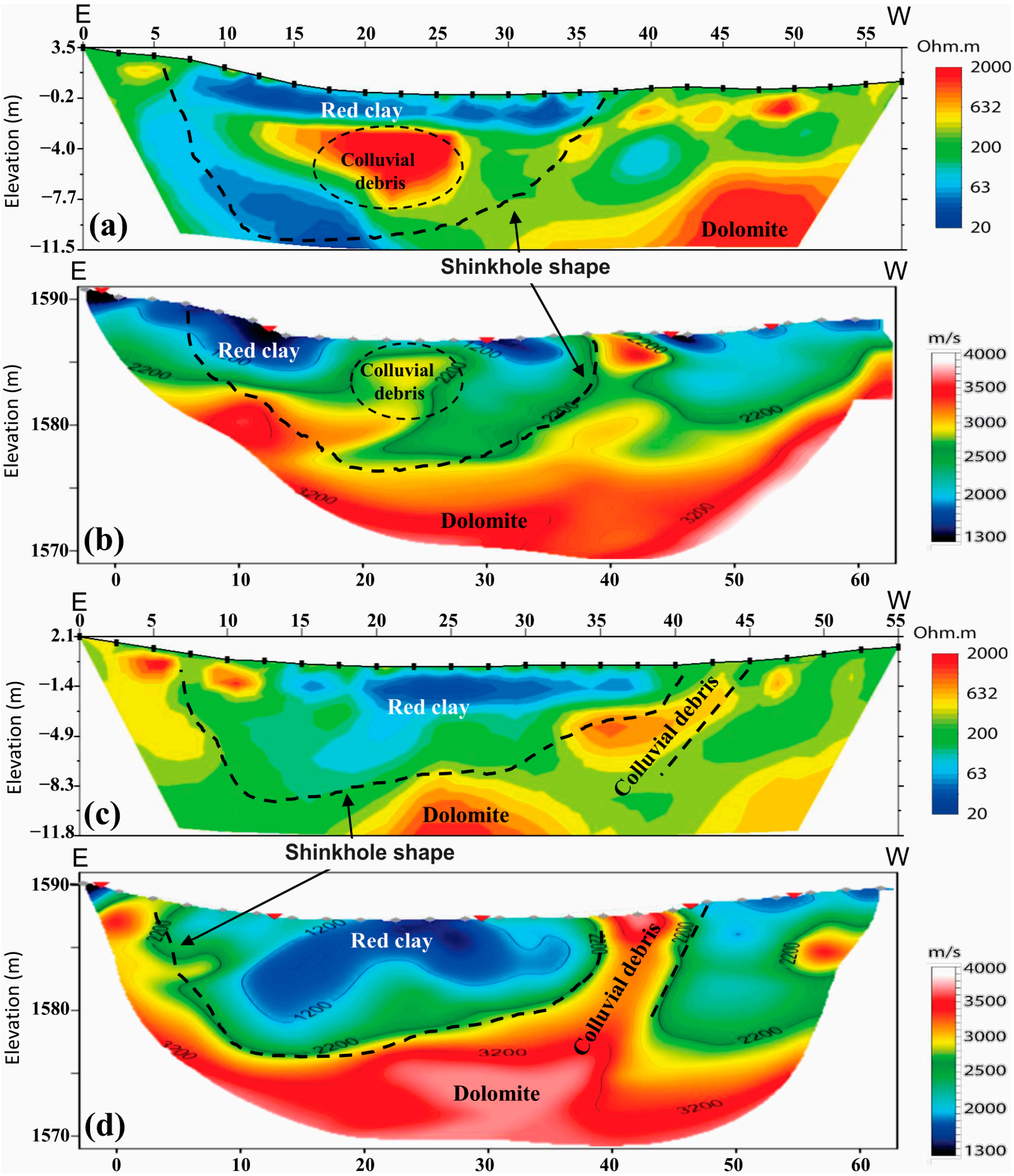

Figure 8. For comprehensive visualization, comparison of ERT and SRT profiles in the same positions, as (**a**) E2 and (**b**) S2, and (**c**) E3 and (**d**) S3. See location of ERT and SRT profiles in Figure 2.

5. Conclusions

The investigation was conducted in the Llano de los Juanes experimental intact karstic system, where anthropogenic activity was absent, ensuring the system's pristine condition, and provided important insights into the geological characteristics of the studied sinkhole and the surrounding areas. The difficult terrain conditions limited the options for implementing additional profiles, but in this case study, the combination of electrical resistivity tomography (ERT) and seismic refraction tomography (SRT) proved effective.

Based on the results of the electrical resistivity tomography, we were able to distinguish between the upper layer of clayey deposits, with minimal resistivity values, and the underlying carbonate deposits unit, which displays high resistivity values. The resistivity data interpretation also revealed the presence of colluvial debris within the conductive layers. Furthermore, we highlighted a transitional zone between these two layers, which had lower resistivity values than the deeper layer and was associated with the fissured shale layer. The seismic data displayed in the SRT 3D Grid effectively identified the shape of the sinkhole by observing the intersections between the profiles, which revealed a progressive increase in velocities with depth. This velocity variation corresponded to the transition from the red clay materials near the surface to the underlying carbonate layer. Notably, the seismic data also emphasized high velocity values within the red clay deposits, which were associated with the colluvial layer of debris. Importantly, these changes in velocity coincided with the boundaries previously identified using electrical resistivity tomography.

Overall, these findings highlight the complex nature of the subsiding area, with differences in clay filling, rooting orientation, and sinkhole formation between the northern and southern parts. More research and analysis are required to fully comprehend the underlying mechanisms and factors that contribute to these asymmetries, as well as to gain a comprehensive understanding of the subsidence processes in this region.

Author Contributions: Conceptualization, O.J. and P.M.-P.; Data curation, O.J. and P.M.-P.; Investigation, O.J., P.M.-P., F.J.A. and M.A.M.-S.; Project administration, M.A.M.-S. and F.J.A.; Resources, F.J.A.; Software, O.J. and M.A.M.-S.; Supervision, D.E.A. and M.A.M.-S.; Validation, O.J. and M.A.M.-S.; Visualization, P.M.-P., D.E.A., M.D.V.-M. and M.C., Writing—original draft, O.J.; Writing—review & editing, O.J., P.M.-P. and F.J.A. All authors have read and agreed to the published version of the manuscript.

Funding: This research received no external funding.

Data Availability Statement: Not applicable.

Conflicts of Interest: The authors declare no conflict of interest.

References

1. Goldscheider, N.; Drew, D. *Methods in Karst Hydrogeology*; CRC Press: Boca Raton, FL, USA, 2007; Volume 28.
2. Jourde, H.; Gabrovsek, F. Epikarst. In *Treatise on Geomorphology*; Karst Geomorphology; Shroder, J.F., Ed.; Elsevier: Amsterdam, The Netherlands, 2013; Volume 6, pp. 201–218.
3. Sweeting, M.M. *Karst Landforms*; Macmillan: London, UK, 1972; p. 362.
4. Bögli, A. *Karst Hydrology and Physical Speleology*; Springer Science & Business Media: Berlin/Heidelberg, Germany, 1980; pp. 131–132.
5. White, W.B. *Geomorphology and Hydrology of Karst Terrains*; Oxford University Press: Oxford, UK, 1988; 464p.
6. Williams, P.W. Dolines. In *Encyclopedia of Caves and Karst Science*; Gunn, J., Ed.; Fitzroy Dearborn: New York, NY, USA; London, UK, 2004; pp. 304–310.
7. Beck, B.F. Soil piping and sinkhole failures. In *Enyclopedia of Caves*; White, W.B., Ed.; Elsevier: New York, NY, USA, 2005; pp. 523–528.
8. Waltham, T.; Bell, F.; Culshaw, M. *Sinkholes and Subsidence*; Springer: Berlin/Heidelberg, Germany, 2005.
9. Gutiérrez, F. Hazards associated with karst. In *Geomorphological Hazards and Disaster Prevention*; Alcántara, I., Goudie, A., Eds.; Cambridge University Press: Cambridge, UK, 2010; pp. 161–175.
10. Nisio, S.; Caramanna, G.; Ciotoli, G. Sinkholes in Italy: First results on the inventory and analysis. In *Natural and Anthropogenic Hazards in Karst Areas: Recognition, Analysis and Mitigation*; Parise, M., Gunn, J., Eds.; Geological Society Special Publication No. 279; Geological Society: London, UK, 2007; pp. 23–45.
11. Parise, M.; Gunn, J. *Geomorphology and Hydrogeology of Karst Terrains*; Oxford University Press: Oxford, UK, 2007.

12. Gutiérrez, F.; Carbonel, D.; Kirkham, R.M.; Guerrero, J.; Lucha, P.; Matthews, V. Can flexural-slip faults related to evaporite dissolution generate hazardous earthquakes? The case of the Grand Hogback Monocline of west-central Colorado. *GSA Bull.* **2014**, *126*, 1481–1494. [CrossRef]
13. Saribudak, M.; Hawkins, A.; Stoker, K. Do Air-Filled Caves Cause High Resistivity Anomalies? A Six-Case Study from the Edwards Aquifer Recharge Zone in San Antonio, Texas. *Houst. Geol. Soc. Bull.* **2012**, *54*, 41–49.
14. Abdallatif, T.; Khafagy, A.S.A.B.; Khozym, A. Geophysical investigation to delineate hazardous cavities in Al-HassaKarstic Region, Kingdom of Saudi Arabia. *Eng. Geol. Soc. Territ.* **2015**, *5*, 507–514.
15. Martinez-Pagan, P.; Gomez-Ortiz, D.; Martin-Crespo, T.; Manteca, J.I.; Rosique, M. The electrical resistivity tomography method in the detection of shallow mining cavities. A case study on the Victoria Cave, Cartagena (SE Spain). *Eng. Geol.* **2013**, *156*, 1–10. [CrossRef]
16. Vouillamoz, J.-M.; Legchenko, A.; Albouy, Y.; Bakalowicz, M.; Baltassat, J.-M.; Al-Fares, W. Localization of karstaquifer with magnetic resonance sounding and resistivity imagery. *J. Ground Water* **2003**, *41*, 578–587. [CrossRef] [PubMed]
17. Boucher, M.; Favreau, G.; Descloitres, M.; Vouillamoz, J.M.; Massuel, S.; Nazoumou, Y.; Legchenko, A. Contribution of Geophysical Surveys to Groundwater Modelling of a Porous Aquifer in Semiarid Niger: An Overview. *Comptes Rendus Geosci.* **2009**, *341*, 10–11. [CrossRef]
18. Jayeoba, A. 2-D Electrical Resistivity Tomography for Groundwater Exploration in Hard Rock Terrain. *Int. J. Sci. Res.* **2015**, *4*, 156–163.
19. Hussain, Y.; Uagoda, R.; Borges, W.; Nunes, J.; Hamza, O.; Condori, C.; Cárdenas-Soto, M. The potential use of geophysical methods to identify cavities, sinkholes, and pathways for water infiltration. *Water* **2020**, *12*, 2289. [CrossRef]
20. Soriano, M.A.; Simón, J.L. Factors of the Dissolution Process. Historical Changes Observed in Doline Distribution, Geological Reconnaissance, Drilling, Local Subsidence Rates, Analysis of Aerial Photographs, and Site Inspection. *Water* **1995**, *28*, 51–74.
21. Soriano, M.A.; Simón, J.L. Estudio de los procesos kársticos en el término municipal de Jerez de los Caballeros (Badajoz). *Boletín Geológico Y Min.* **1997**, *108*, 487–505.
22. Casas, A.M.; Mochales, T.; Pueyo, E.L.; Soriano, M.A.; Pueyo, Ó.; Pocoví, A. La prospección geofísica en áreas urbanas como instrumento para la cartografía de riesgos kársticos. In *Libro de Resúmenes de la Conferencia Regional, Cartografía Geológica Aplicada a Áreas Urbanas. O Caso da Área Metropolitana de Lisboa*; Nunes da Costa, C., Ed.; Universidade de Lisboa: Lisbon, Portugal, 2006; pp. 156–166.
23. Kaufmann, G. Geophysical Mapping of Solution and Collapse Sinkholes. *J. Appl. Geophys.* **2014**, *111*, 271–288. [CrossRef]
24. Butler, D.K. Detection and Characterization of Subsurface Cavities, Tunnels and Abandoned Mines. *Near Surf. Geophys. Hum. Act. Sci.* **2008**, *1*, 578–584.
25. Hauck, C.; Kneisel, C.; Rudolph, S. Geophysical methods in permafrost research: Current use and future potential. *Permafr. Periglac. Process.* **2020**, *31*, 222–238.
26. Strozyk, F.; Gosselin, C.; Chaput, M.; Ménard, Y.; Samson, C. Geophysical characterization of a landfill using electrical resistivity tomography (ERT): A case study from Quebec, Canada. *Environ. Earth Sci.* **2019**, *78*, 332.
27. Gao, Y.; Li, Y.; Hu, X. Geophysical characterization of sinkhole-prone areas in karst regions using ground penetrating radar and electrical resistivity tomography. *Environ. Earth Sci.* **2021**, *80*, 1–11.
28. Jaafar, O.; Ibrahim, Z.; Saad, R.; Sia, L.K. Electrical resistivity imaging and ground-penetrating radar surveys for sinkhole detection in karstic terrain. *Environ. Earth Sci.* **2020**, *79*, 1–15.
29. Han, Y.; Wang, X.; Li, J.; Huang, Q.; Wu, Y. Combined use of ground-penetrating radar and electrical resistivity tomography for sinkhole detection in karst areas. *J. Appl. Geophys.* **2019**, *168*, 155–164.
30. Sheehan, J.R.; Doll, W.E.; Watson, D.B.; Mandell, W.A. Application of Seismic Refraction Tomography to Karst Cavities. In Proceedings of the US Geological Survey Karst Interest Group, Rapid City, SD, USA, 12–15 September 2005; pp. 29–38.
31. Valois, R.; Bermejo, L.; Guérin, R.; Hinguant, S.; Pigeaud, R.; Rodet, J. Karstic morphologies identified with geophysics around Saulges caves (Mayenne, France). *Archaeol. Prospect.* **2010**, *17*, 151–160. [CrossRef]
32. Riddle, J.D.; Slater, L.D.; Guertal, W.R.; Sholar, J.R. Application of electrical resistivity tomography and time domain reflectometry for detection of sinkholes and anomalous zones at a closed landfill. *J. Appl. Geophys.* **2010**, *70*, 244–255.
33. Gan, H.; Jiang, Y.; Hu, J.; Chen, S.; Lin, H. Detection and spatial analysis of subsidence using electrical resistivity tomography in an area of reclamation land affected by underground coal mining. *Mine Water Environ.* **2017**, *36*, 223–230.
34. Rinaldi, V.A.; Ibarra, H.V.; Viguera, R.F.; Harasimiuk, J.C. Application of Seismic Tomography for Detecting Structural Faults in a Tertiary Formation. *E3S Web Conf.* **2019**, *92*, 18008. [CrossRef]
35. Ariff, M.A.M.; Hashim, M.; Yusoff, Z.M.; Ghazali, A.H. Investigating the morphology and filling material of a sinkhole using geoelectrical resistivity imaging: A case study in Kuala Lumpur, Malaysia. *Environ. Earth Sci.* **2016**, *75*, 804.
36. Wang, Y.; Liu, Q.; Zhou, Z.; Dong, C. Geophysical exploration of sinkholes in karst areas: A review. *J. Appl. Geophys.* **2019**, *167*, 80–94.
37. Molina, J.; Pedrera, A.; Galindo-Zaldívar, J.; González-Castillo, L.; Ruiz-Constán, A. The Sierra de Gádor: A key segment for understanding the Neogene-Quaternary tectonics of the eastern Betics (SE Spain). *Geol. Acta* **2012**, *10*, 1–23.
38. Contreras, E.; Delgado, J.; Jiménez, P.; Bolívar, J.P. Hydrogeological characterization of karst aquifers: An example of the Sierra de Líjar (Southern Spain). *Environ. Geol.* **2008**, *55*, 1015–1026.

39. Pulido-Bosch, A.; Carrasco, F.; Sanz de Galdeano, C.; López-Geta, J.A. Hydrogeological characterization of carbonate aquifers in a Mediterranean mountainous area (Sierra de Gádor, SE Spain). *Hydrogeol. J.* **2000**, *8*, 405–416.
40. Martín Rojas, I. Las Unidades Internas del sector de la sierra de Gádor: Estructura y Evolución Geodinámica. Ph.D. Thesis, Universidad de Alicante, Alicante, Spain, 2006.
41. Dominguez-Castro, F. Contribution of environmental isotopes to the hydrogeological knowledge of a karst aquifer in a semi-arid region (Campo de Dalias, SE Spain). *Isot. Environ. Health Stud.* **2000**, *36*, 237–253.
42. Marín-Lechado, C.; Jiménez-Sánchez, M.; Rossi, P. Integrated use of electrical resistivity tomography and hydrochemical data to characterize a saline intrusion in a coastal aquifer (Granada, SE Spain). *Hydrogeol. J.* **2005**, *13*, 133–144.
43. Alonso-Zarza, A.M.; Silva, P.G.; Martín-Pérez, A. Palaeoenvironmental significance of palustrine carbonates and calcretes in an intramontane basin: The case of the Miocene of the Granada Basin (SE Spain). *Sedimentology* **2002**, *49*, 137–154.
44. García-Castellanos, D.; Villaseñor, A. Messinian salinity crisis regulated by competing tectonics and erosion at the Gibraltar arc. *Nature* **2011**, *480*, 359–363. [CrossRef]
45. Oyonarte, C.; Valero-Garcés, B.; Delgado, J. Hydrochemical and isotopic characterisation of groundwater in a karstic area: The Sierra de Líjar (Southern Spain). *Hydrol. Earth Syst. Sci.* **1998**, *2*, 25–35.
46. Alcalá, F.J.; Andreo, B.; Carrasco, F.; Pulido-Bosch, A. Karst in gypsum of Sorbas (SE Spain): Hydrogeological behavior and hazards. *Geomorphology* **2011**, *134*, 207–220.
47. Li, X.Y.; Contreras, S.; Solé-Benet, A. Unsaturated hydraulic conductivity in limestone dolines: Influence of vegetation and rock fragments. *Geoderma* **2008**, *145*, 288–294. [CrossRef]
48. Cantón, Y.; Villagaría, L.; Moro, M.J.; Serrano-Ortiz, P.; Were, A.; Alcalá, F.J.; Kowalski, A.S.; Solé-Benet, A.; Lázaro, R.; Domingo, F. Temporal dynamics of soil water balance components in a Mediterranean carbonate range in SE Spain: Estimation of potential recharge. *Hydrol. Sci. J.* **2010**, *5*, 737–753. [CrossRef]
49. Bano, M.; Hasan, M.A.; Bakht, M.; Nawaz, A.; Islam, N. 2D resistivity imaging of subsurface sediments and identification of groundwater contamination in the vicinity of a landfill site. *Environ. Earth Sci.* **2018**, *77*, 233.
50. Dahlin, T.; Loke, M.H. Resolution of 2D Wenner resistivity imaging as assessed by numerical modelling. *J. Appl. Geophys.* **1998**, *38*, 237–248. [CrossRef]
51. Binley, A.; Kemna, A.; Cassiani, G. Electrical methods for imaging and monitoring subsurface processes. *Geophys. Res. Lett.* **2006**, *33*, 18.
52. Dahlin, T.; Zhou, B. Multiple-gradient array measurements for high-resolution imaging of the vadose zone. *J. Environ. Eng. Geophys.* **2004**, *9*, 131–144.
53. Loke, M.H.; Barker, R.D. Rapid least-squares inversion of apparent resistivity pseudosections by a quasi-Newton method. *Geophys. Prospect.* **1996**, *44*, 131–152. [CrossRef]
54. Advanced Geosciences, Inc. *AGI Earthimager 2D, Software*; Advanced Geosciences, Inc.: Houston, TX, USA, 2022.
55. Dahlin, T.; Bernstone, C. A roll-along technique for 3D resistivity data acquisition with multi-electrode arrays. In Proceedings of the Symposium on the Application of Geophysics to Engineering and Environmental Problems, Reno, NV, USA, 23–26 March 1997; Volume 2, pp. 927–935.
56. Kuniansky, E.L. *Groundwater Resource Assessment*; CRC Press: Boca Raton, FL, USA, 2005.
57. Sarmiento, C.; Hernandez, W.; Segura, P.; Bernal, A. 2D Seismic Refraction Imaging of the Shallow Subsurface at the Tempisque River Basin, Guanacaste Province, Costa Rica. *Pure Appl. Geophys.* **2020**, *177*, 2695–2710.
58. Yan, Y.; Hao, Q.; Cheng, Y.; Cai, S.; Liu, J.; Qiu, N.; Yang, J. Fault detection by seismic refraction tomography in Guanling fault zone, Guizhou Province. *Chin. J. Geophys.* **2017**, *60*, 1124–1134.
59. *SUMMIT II Compact*; DMT Group: Essen, Germany, 2020; pp. 1–2. Available online: https://www.summit-system.de/fileadmin/redaktion/microsites/summitsystem/Brochures/PB_SUMMIT_II_Compact.EN_01.20.pdf (accessed on 22 May 2023).
60. Telford, W.M.; Geldart, L.P.; Sheriff, R.E.; Keys, D.A. *Applied Geophysics*, 2nd ed.; Cambridge University Press: Cambridge, UK, 1990.
61. Chouteau, M.; Mareschal, M.; Giroux, B.; Lines, L. Seismic Refraction Tomography Using Forward Finite Difference Modeling and Waveform Inversion: Application to a Mineral Exploration Site in Quebec, Canada. *Geophys. J. Int.* **2004**, *157*, 537–548.
62. Schuster, G.T. Three-dimensional traveltime computation using eikonal tomography. *Geophysics* **1993**, *58*, 1158–1166.
63. Hagedoorn, J.G. Propagation of elastic waves in multi-layered media. *J. Appl. Phys.* **1959**, *30*, 1558–1567.